2016

Patterning the Condenser-Side Wick in Ultra-Thin Vapor Chamber Heat Spreaders to Improve Skin Temperature Uniformity of Mobile Devices

G Patakar
Purdue University

Justin Weibel
Purdue University, jaweibel@purdue.edu

S V. Garimella
Purdue University, sureshg@purdue.edu

Patakar, G; Weibel, Justin; and Garimella, S V., "Patterning the Condenser-Side Wick in Ultra-Thin Vapor Chamber Heat Spreaders to Improve Skin Temperature Uniformity of Mobile Devices" (2016). *CTRC Research Publications.* Paper 308.
http://dx.doi.org/10.1016/j.ijheatmasstransfer.2016.05.093

Patterning the Condenser-Side Wick in Ultra-Thin Vapor Chamber Heat Spreaders to Improve Skin Temperature Uniformity of Mobile Devices

Gaurav Patankar, Justin A. Weibel and Suresh V. Garimella*

Cooling Technologies Research Center, an NSF I/UCRC
School of Mechanical Engineering, Purdue University
585 Purdue Mall, West Lafayette, IN 47907 USA

Abstract

Vapor chamber technologies offer an attractive approach for passive heat spreading in mobile electronic devices, in which meeting the demand for increased functionality and performance is hampered by a reliance on conventional conductive heat spreaders. However, market trends in device thickness mandate that vapor chambers be designed to operate effectively at ultra-thin (sub-millimeter) thicknesses. At these form factors, the lateral thermal resistance of vapor chambers is governed by the saturation temperature/pressure gradient in the confined vapor core. In addition, thermal management requirements of mobile electronic devices are increasingly governed by user comfort; heat spreading technologies must be designed specifically to mitigate hot spots on the device skin. The current work considers these unique transport limitations and thermal requirements encountered in mobile applications, and develops a methodology for the design of vapor chambers to yield improved condenser-side temperature uniformity at ultra-thin form factors. Unlike previous approaches that have focused on designing evaporator-side wicks for reduced thermal resistance and delayed dryout at higher operating powers, the current work focuses on manipulating the condenser-side wick to improve lateral heat spreading. The proposed condenser-side wick designs are evaluated using a 3D numerical vapor chamber

* Corresponding author: Tel. 765 494 5621 ; sureshg@purdue.edu

transport model that accurately captures conjugate heat transport, phase change at the liquid-vapor interface, and pressurization of the vapor core due to evaporation. A biporous condenser-side wick design is proposed that facilitates a thicker vapor core, and thereby reduces the condenser surface peak-to-mean temperature difference by 37% relative to a monolithic wick structure.

Keywords: mobile device thermal management, vapor chamber, heat pipe, ultra-thin, sintered wick, patterned condenser wick

Nomenclature

V	velocity [m s^{-1}]
x, y, z	Cartesian coordinates [m]
r	radius [m]
u	x-velocity [m s^{-1}]
u_{eff}	effective x-velocity [m s^{-1}]
v	y-velocity [m s^{-1}]
w	z-velocity [m s^{-1}]
P	pressure [Pa]
P_{cap}	capillary pressure [Pa]
K	permeability [m^2]
K_{eff}	effective permeability [m^2]
C_E	Ergun's coefficient [–]
T	temperature [K]

C	specific heat capacity [J kg^{-1} K^{-1}]
k	thermal conductivity [W m^{-1} K^{-1}]
k_{eff}	effective thermal conductivity [W m^{-1} K^{-1}]
h_{fg}	enthalpy of vaporization [J kg^{-1}]
A	area [m^2]
m	mass flow rate [kg s^{-1}]
R	gas constant [J kg^{-1} K^{-1}]
Q	power (rate of heat flow) [W]
h	convection coefficient [W m^{-2} K]
t_{wick}	wick thickness [m]
W	groove width [μm]
n	extrapolation coefficient [–]
n_t	number of transient steps between extrapolations [–]
d	sintered copper particle diameter [m]

Greek symbols

ρ	density [kg m^{-3}]
ϕ	porosity [–]
μ	dynamic viscosity [Pa s]
σ	accommodation coefficient [–]
γ	surface tension [N m^{-1}]

Subscripts

i	wick–vapor interface
0	reference

solid	solid properties
liquid	liquid properties
vapor	vapor properties
wick	wick properties
s	condenser surface
m	mean
amb	ambient

Superscripts

″	per unit area

1. Introduction

A vapor chamber passively transports heat from a localized source to a much larger heat rejection surface. Vapor chambers are used to mitigate the temperature rise of sensitive components in the cooling of electronics by spreading heat away from local hot spots. The sealed vapor chamber (Figure 1) encloses a working fluid. Vapor is generated at the evaporator section located over the heat source and driven into the rest of the chamber. The vapor condenses on the inner surface of the opposing wall where heat is rejected. A porous wick passively pumps the condensed liquid back to the evaporator. Mobile electronic devices such as smartphones and tablets are trending toward lower thickness and higher functionality, leading to higher heat generation density from active components. It is not practical to use active air cooling methods or embed large, finned heat sinks, due to the size constraints. Thus, to minimize the temperature rise of components and surfaces to be cooled by natural convection, heat must be spread uniformly over the device surface. Ultra-thin vapor chambers may offer a viable solution for passive spreading within mobile devices.

Recent research in vapor chamber design has focused on high-performance commercial and military electronics that require heat spreaders capable of dissipating high heat fluxes (over 500 W/cm^2) from small areas [1]. At such high heat fluxes, the wall superheat typically induces nucleate boiling in the evaporator wicks. Vapor chamber designs for these applications focus on tailoring the evaporator wick to tolerate operation in the boiling regime without suffering from dryout, in order to take advantage of the reduced evaporator thermal resistance that is characteristic of boiling heat transfer. Wick design strategies in the literature have analyzed the ability of wicks to evacuate vapor bubbles generated during boiling in order to avoid dryout and reduce the thermal resistance [2]. This has been achieved through patterning the wick structure

[3] or using biporous wicks [4] to enable continuous feeding of liquid to the evaporator under boiling conditions. Alternate strategies aim to reduce the evaporator wick thermal resistance and preserve operation in the evaporative regime (avoiding boiling) using thin nanostructure arrays [5, 6] or thin monoporous copper particles with arterial liquid return paths [7, 8].

The requirements of vapor chambers for mobile thermal management are in stark contrast to these high-power-density applications. For mobile applications, vapor chambers must be ultra-thin, on the order of less than 1 mm, and typically operate at significantly lower power inputs and heat fluxes. At such thicknesses and heat fluxes, the thermal resistances across the vapor chamber wall and wick are very low while the lateral temperature gradient in the confined vapor core governs the heat spreading resistance [9]. Boiling is not likely to occur in the evaporator wick. Thus, the design focus for mobile applications must shift away from the evaporator wick structure and toward the layout of the wick and vapor domains. There is a fledgling body of literature that has investigated the design of ultra-thin heat pipes or vapor chambers. Aoki *et al.* [10] fabricated heat pipes with thickness less than 1 mm by simply flattening traditional cylindrical grooved heat pipes. Ding *et al.* [11] developed a titanium-based vapor chamber with a thickness of 0.6 mm that included a uniform array of microfabricated titanium pillars as the wick structure. Oshman *et al.* [12] fabricated a 1 mm-thick heat pipe with a hybrid copper mesh and micropillared wick encased in a liquid-crystal polymer chamber. Lewis *et al.* [13] fabricated a 0.5 mm-thick flexible heat pipe made of copper-cladded polyimide, with a copper mesh wick. In each of these studies, the wick was designed to allow dissipation of the maximum possible power and/or minimum evaporator-to-condenser thermal resistance at an ultra-thin form factor.

A unique objective of the vapor chamber design process for mobile applications is condenser-side surface temperature uniformity, in contrast to a sole objective of reducing

evaporator temperature. The condenser surface is in close proximity to the user's skin and may not propagate hotspots generated within the device. Overly high device skin temperature is often the factor which forces limits on mobile electronic device performance, rather than the junction temperatures [14].

The current work focuses on the design of ultra-thin vapor chambers for improved condenser-surface temperature uniformity; consideration of this application-driven design constraint is unique to this work. A 3D numerical vapor chamber transport model is utilized to analyze the proposed vapor chamber wick domain layouts. The enhanced temperature uniformity produced by different candidate condenser-side wick designs are compared against a baseline design having a homogeneous, uniform wick layer.

2. Modeling Approach

2.1. Numerical vapor chamber transport model

The numerical modeling methodology used in the current work is adapted from Vadakkan *et al.* [15] and was previously validated against experimental data by Ranjan *et al.* [16]. The model solves the governing continuity and momentum equations in the wick and vapor core, and the energy equation in the wall, wick, and vapor core of the vapor chamber. The continuity equation is

$$\varphi \frac{\partial \rho}{\partial t} + \nabla \cdot (\rho V) = 0 \tag{1}$$

in which the $\partial\rho/\partial t$ term accounts for the mass addition and depletion in the wick and vapor core, and φ is the porosity of the zone with $\varphi = 1$ in the vapor core. The momentum equations are

$$\frac{\partial \rho u}{\partial t} + \nabla \cdot (\rho V u) = -\frac{\partial \varphi P}{\partial x} + \nabla \cdot (\mu \nabla u) - \frac{\mu \varphi}{K} u - \frac{C_E \varphi}{K^{1/2}} \rho |V| u \tag{2}$$

$$\frac{\partial \rho v}{\partial t} + \nabla \cdot (\rho V v) = -\frac{\partial \varphi P}{\partial y} + \nabla \cdot (\mu \nabla v) - \frac{\mu \varphi}{K} v - \frac{C_E \varphi}{K^{1/2}} \rho |V| v \tag{3}$$

$$\frac{\partial \rho w}{\partial t} + \nabla \cdot (\rho V w) = -\frac{\partial \varphi P}{\partial z} + \nabla \cdot (\mu \nabla w) - \frac{\mu \varphi}{K} w - \frac{C_E \varphi}{K^{1/2}} \rho |V| w \tag{4}$$

in which K is the permeability of the zone. In the vapor core, $K = \infty$. The third and fourth terms in the momentum equations represent the Brinkman–Forchheimer extended Darcy model. The energy equation is

$$\frac{\partial (\rho C) T}{\partial t} + \nabla \cdot [(\rho C) V T] = \nabla \cdot (k_{eff} \nabla T) \tag{5}$$

in which (ρC) assumes different values in different zones: in the wall $(\rho C) = (\rho C)_{solid}$, in the wick $(\rho C) = \varphi (\rho C)_{liquid} + (1 - \varphi)(\rho C)_{solid}$, and in the vapor core $(\rho C) = (\rho C)_{vapor}$.

At the wick–vapor interface, an energy balance that accounts for conduction, convection, and phase change is applied to obtain the interface temperature T_i:

$$-k_{wick} A_i + m_i C_{liquid} T_i = -k_{vapor} A_i + m_i C_{vapor} T_i + m_i h_{fg} \tag{6}$$

in which a negative value of m_i indicates evaporation while a positive value indicates condensation. The Clausius-Clapeyron relation yields the interface pressure P_i, using some arbitrary reference pressure and temperature (P_0, T_0):

$$\frac{R}{h_{fg}} \ln\left(\frac{P_i}{P_0}\right) = \frac{1}{T_0} - \frac{1}{T_i} \ . \tag{7}$$

The evaporation/condensation mass flux at the interface is computed using a relation (Schrage [17]) based on kinetic theory of gases:

$$m_i'' = \left(\frac{2\sigma}{2-\sigma}\right)\left(\frac{1}{(2\pi R)^{1/2}}\right)\left(\frac{P_{vapor}}{T_{vapor}^{1/2}} - \frac{P_i}{T_i^{1/2}}\right). \tag{8}$$

While the literature does not offer an established theoretical value for the accommodation coefficient (a wide range of experimental and theoretical values have been reported [18]), σ is chosen to be 0.03 for the current work. It is noted for the current work that the temperature difference at the wick–vapor interface is negligible compared to the overall temperature difference in the vapor chamber; the value of the accommodation coefficient chosen therefore does not affect the primary conclusions. The evaporation/condensation process connects the vapor core and wick domains. The vapor phase density change caused by pressurization due to heating is computed using the ideal gas law. All flows are assumed laminar and incompressible. The wick is assumed to be always saturated, and the change in the liquid mass by evaporation or condensation is taken into account by adjusting the density (while keeping the volume constant), rather than by tracking the evolution of the liquid–vapor interface. A damping coefficient is used to under-relax the evaporation/condensation mass and energy source/sink terms during convergence within a time step to suppress numerical instabilities.

The governing equations are solved using the commercial finite-volume software FLUENT [19]; the interfacial transport equations are implemented using an additional script (termed as a user defined function). The PISO algorithm is used for pressure–velocity coupling, which allows use of larger time-steps in the transient solution. First-order discretization is used for the continuity and momentum equations (for numerical stability), while the energy equation uses second-order discretization. The transient formulation is first-order implicit.

2.2. Steady-state-seeking solution algorithm

The numerical model has an inherently high computational cost. Thermophysical vapor properties and the evaporation/condensation mass flux are sensitive to temperature; thus, the

hydrodynamics are coupled to the energy transport. In addition, the energy and mass source terms associated with phase change are damped for numerical stability. These factors increase the computational cost for iterative solvers. The cost is exacerbated by the extreme geometric aspect ratios to be investigated for mobile electronics, which require a high cell count in the computational mesh. A steady-state-seeking solution algorithm is developed to facilitate tractable simulation of the geometries investigated herein.

The model is inherently transient and the thermal performance metrics of interest to the current study are obtained by simulating in time until steady-state conditions are achieved. Given that the transient path is not of direct interest, the computational cost can be reduced by minimizing the number of time steps required to reach the steady-state conditions. This is achieved by forecasting the variable values for every cell in the mesh; a linear extrapolation (forward in time) is performed based on the values of each variable at consecutive transient time steps. This extrapolation process jumps to a solution that is closer to steady state without actually going through the physical transient path. It is noted that the intermediate faux-transient solutions obtained from such extrapolations do not represent the actual transient behavior. After multiple such extrapolations, the solution tends to the physical steady state. The steady-state-seeking algorithm is implemented as follows:

1. Initialize variables: velocities are set to zero in the domain and the global temperature is set to an average of the condenser surface, computed using $Q = h \cdot A_s \cdot \left(T_{s,m} - T_{amb} \right)$.
2. Run the simulation for n_t transient time steps.
3. Linearly extrapolate the flow variables (ρ, u, v, w, T) in each cell using the last two transient data points with an extrapolation coefficient n such that $T_{new} = n \cdot \left(T_1 - T_0 \right) + T_1$.
4. Set the variable values to the extrapolated solution.

5. Repeat steps 2-4 until the solution converges to steady state.

Controls need to be applied for the choice of values n_t and n to ensure efficient convergence to steady state. The mean evaporator temperature over the area of heat input is used as the primary control variable. The mean evaporator temperature will always be higher than the initialized value of the mean condenser surface temperature. After an extrapolation of the evaporator temperature toward steady-state conditions and away from the initialized value, it is observed that this evaporator temperature may regress back toward the initial guess value for a few subsequent transient steps. This behavior is expected due to the approximate nature of the linear extrapolation used to forecast the behavior of the nonlinear system. The value of n_t is chosen to ensure that there is a sufficient number of solution steps so that the evolution of the evaporator temperature continues toward the steady-state conditions before another extrapolation is made. The value of n directly affects simulation time. If the value is set too high, the evaporator temperature jumps beyond the steady-state value (unknown *a priori*); this significantly extends the simulation time as the algorithm becomes inactive while the temperature reverts to the ultimate steady-state value. An overly low value of n would increase the number of extrapolation steps in the algorithm and thus also increase the simulation time. The value of n depends on the individual case being simulated, and an intermediate value that minimizes the simulation time is chosen heuristically. Because the various solutions steps do not lie on the actual transient solution, typical methods of tracking steady-state conditions (*e.g.*, change in temperature at key locations) cannot be used. In this case, therefore, the difference between the input power at the evaporator and the condenser is tracked. Steady state is considered to be reached when this difference reaches 0.1% of the constant input power.

The algorithm is demonstrated using a 2D vapor chamber geometry for which obtaining the full transient simulation is computationally feasible for comparison. The 2D geometry and case details (Figure 2) are taken from Ref. [20]. The external dimensions are 30 mm × 3 mm, with a uniform copper wall thickness of 0.25 mm and a uniform wick thickness of 0.2 mm; the wick has porosity, permeability, and effective conductivity of 0.56, 2.97×10^{-11} m^2, and 40 W/mK, respectively. The evaporator (heat input of 10 W/m^2) is on one flat side, with a width of 5 mm, while the entire area of the opposing flat side is the condenser (convection coefficient of 400 W/m^2K and ambient temperature of 298 K). The side walls are adiabatic. The working fluid is water. The numerical mesh has ~16,000 rectilinear cells with aspect ratios of ~1. Figure 3 compares the evaporator mean temperature and the evaporator-to-condenser power difference along the solution path for simulations with and without the steady-state-seeking solution algorithm implemented. For this case, the algorithm uses a value of 50 for the extrapolation coefficient *n*. In Figure 3a, it can be seen that the simulation proceeds towards the steady state much faster with the algorithm implemented due to the intermediate extrapolations in the solution. The inset in Figure 3a shows the jumps in the evaporator temperature for each extrapolation. It can also be seen, for some cases, that after the jump, the evaporator temperature deviates from the steady state. Hence the algorithm does not extrapolate till the evaporator temperature evolves toward the steady state (*i.e.*, away from the initial guess value). Figure 3b shows the evaporator-to-condenser power difference along the solution path, which is tracked for confirming steady state. The algorithm reduces the required number of solution steps from 700 to 37, representing an order-of-magnitude reduction in the computational cost.

The computational cost reduction offered by the steady-state-seeking solution algorithm allows for tractable simulation of high-aspect-ratio 3D vapor chamber geometries. The algorithm

is implemented for all subsequent 3D simulations discussed in this work. The 3D simulations were performed using 16-core parallel processing (two 8-core Intel Xeon-E5 with 32 GB memory) to achieve a simulation time for each case on the order of one day.

3. Design Objective

We investigate the heat spreading performance of ultra-thin vapor chambers with boundary conditions that simulate the cooling of a mobile electronics device. The vapor chamber is used to spread heat from a local source to a condenser side close to the surface of the device, where heat is rejected by natural convection. Any ergonomics-based thermal performance metric, used to assess vapor chamber designs, would be governed by the condenser-side surface temperatures. The temperature distributions illustrated in Figure 4 are a schematic representation of temperatures along a rake on the condenser-side surface of a thin vapor chamber under the boundary conditions of interest (informed by experimental observations in Patankar *et al.* [21]). It is important to note that the area-averaged temperature on the condenser surface is independent of the vapor chamber design: for a constant power input and convective boundary conditions, the mean condenser-surface temperature is fixed as $T_{s,m} = Q/hA + T_{amb}$. While natural convection coefficients would vary with the local surface temperature, a constant value has been assumed for the current work due to the relatively small variations in temperature across the surface. The ideal flat profile at the mean temperature shown in Figure 4 can only be achieved if the vapor chamber has no lateral thermal resistance (*i.e.*, if heat could spread laterally without a temperature difference); this profile yields the minimum peak (condenser-surface) temperature. Thus, the objective of vapor chamber designs for ergonomics-driven mobile devices is to minimize the condenser-side peak-to-mean temperature difference, which is equivalent to

obtaining the flattest possible temperature profile. In the current work, the effectiveness of designs (compared at identical boundary conditions) is based on this metric of the peak-to-mean temperature difference on the condenser-side surface.

4. Results and Discussion

A disc-shaped vapor chamber is considered so as to exploit axial symmetry to simplify the simulation domains, and thus maintain a low computational cost (Figure 5a). The disc has a radius of 45 mm and thickness of 0.5 mm. On the evaporator side, the vapor chamber receives heat input over a central circular area with radius of 5 mm. The opposite condenser-side face of the vapor chamber is exposed to a heat transfer coefficient representative of natural convection to the ambient (h = 30 W/m^{2}K and T_{amb} = 298.15 K). The operating power is fixed at 5 W.

When designing the internal configuration of the wall, wick, and vapor space in a vapor chamber, our approach assumes that the external envelope defined above is fixed. The copper wall thickness is held constant at 0.2 mm; in practice, the wall thickness would be selected for structural integrity at the vapor core pressure (determined based on the working fluid and operating temperature). The working fluid used is water. Thus, the flexibility for design enhancements lies in modifying the layout of the wick and vapor domains within the remaining 100 μm of allotted thickness. The current work assumes that the wick is composed of sintered copper powder with 60% open porosity and an effective conductivity of 40 W/mK. The permeability is computed using the relation $\varphi^3 d^2 / 150(1-\varphi)^2$, where d is the particle diameter and φ is the porosity. The wick thickness is ensured to be at least 3 times the particle diameter.

Due to the high aspect ratio of the geometry, an orthogonal meshing scheme is used to avoid highly skewed cells. There are three cells across the wick thickness, ten across the vapor core,

and five across the wall. The aspect ratio of the cells (lateral to normal direction) is highest in the vapor core (ranging from 15 to 20, depending on the case).

4.1. Baseline wick domain design

The baseline design considered is a monolithic wick layer of constant thickness on all internal surfaces of the vapor chamber (Figure 5b and c). The baseline case has a wick thickness of 30 µm composed of 7 µm-diameter copper particles. This minimum possible wick thickness is chosen such that the wick can just support the pressure drop in the system by capillary pressure at the 5 W of heat input; a factor of safety of 2 is used (*i.e.*, the capillary pressure in the wick is twice the total pressure drop in the wick and the vapor core). A minimized wick thickness yields the maximum possible vapor core cross-sectional flow area to minimize the lateral heat spreading resistance. The saturation temperature gradient in the radial direction in the vapor-core is proportional to the pressure drop. A higher cross-sectional flow area reduces the pressure drop, and hence the lateral temperature drop in the vapor-core, reducing the lateral heat spreading resistance. The axisymmetric baseline case was simulated using the numerical model. The results from the simulation are shown in Figure 6 and Figure 7; Figure 6 shows contour plots of the field variables on the axisymmetric plane and Figure 7 shows extracted profiles at key locations.

Interrogation of the thermal and hydrodynamic behavior of the baseline case helps understand the limiting transport mechanisms that can be targeted by design modifications. Figure 6a shows the temperature field in the vapor chamber. The maximum temperature occurs at the centroid of the heat input. The temperature difference across the thickness is much lower than across the lateral extent. The conduction thermal resistances across the wall and wick are comparatively low due to their small thicknesses. Conversely, the thin vapor core induces a high

lateral pressure drop and saturation temperature gradient, leading to the relatively larger lateral temperature variation observed. Figure 6b shows the velocity magnitude in the wick. On the condenser side, the velocity magnitude increases in the outward radial direction in the zone directly above the evaporator; in this region, the amount of liquid flow rate added to the wick by condensation outweighs the increasing area for flow. At regions further away from the center, where the condensation flux is reduced, the outward radial velocity decreases as the flow area increases. A complementary trend is observed in the evaporator wick: in regions beyond the active heat input zone where liquid loss due to evaporation is low, the velocity magnitude increases as the central axis is approached because the flow area decreases. Once in the heated evaporator region, however, the inward radial velocity decreases as the amount of liquid flow in the wick is drastically reduced due to evaporative loss. The pressure field in the wick is shown in Figure 6c; the pressure gradient is clearly proportional to the velocity magnitude in the wick. Figure 6d show the contours of velocity in the vapor core. It can be seen that the velocity magnitude is zero at the axis, and increases sharply in the radial direction to a high value till the maximum radius of the heat input. Outside the heat input region, the velocity magnitude reduces drastically in the outward radial direction. This is caused by the increasing area for vapor flow and by condensation, both of which reduce the vapor mass flux in the outward direction. This gradient of velocity is proportional to the pressure gradient in the vapor core (see the pressure field in Figure 6e).

Figure 7a plots the radial variation of temperature on the condenser-side surface. The shape of this temperature profile is identical to the local heat flux leaving the condenser surface (see right vertical axis of Figure 7a) due to the assumption of a constant heat transfer coefficient to a constant-temperature ambient. This heat flux profile is indicative of the relative thermal

resistance from the evaporator to each location on the condenser surface. For example, consider two heat flow paths, one passing through the center of the condenser surface and the other near the outer circumference. Near the center, heat must only conduct across the walls and wicks; there is a higher thermal resistance to heat passing through the peripheral path due to the saturation temperature gradient in the vapor core. Thus the condenser-surface heat flux and temperature are higher near the center. In order to improve the temperature uniformity on the condenser surface, the resistances along these pathways must be equalized, either by (1) reducing the vapor-core thermal resistance or (2) increasing the condenser-side wall and wick conduction resistances near the center of the vapor chamber. In the following sections we demonstrate how these thermal resistances may be manipulated by modifying the layout of the condenser-side wick in order to achieve improved consider-surface temperature uniformity.

It is important to note that the capillary pressure ($P_{cap} = 2\gamma/(0.21d)$) driving the liquid from the condenser to the evaporator through the wick is the maximum possible pressure drop in the wick. The pressure drop in the wick in this baseline design (Figure 7b) is half of the capillary pressure (since a factor of safety of 2 is used as mentioned earlier). Modified condenser-side wick designs that lead to a wick pressure drop that is lower than 50% of the capillary pressure would indicate that the vapor chamber can operate at a lower wick thickness, allowing an increase in the vapor-core thickness and reduction in the lateral thermal resistance.

The heat flux at the condenser-side wick–vapor interface (proportional to the mass flux due to condensation) is plotted in Figure 7c. Similar to the condenser surface, the heat flux is high near the center and lower at the periphery. It is noted that the net heat transport rate across the wick–vapor interface is the same as that across the condenser outer surface. This heat flux is useful to track because the profile is more sensitive to modifications of the condenser-side wick

compared to the condenser outer surface where the profile is smeared due to conduction in the condenser wall.

4.2. Grooved condenser wick domain design

Two potential approaches were identified in section 4.1 for achieving a more uniform condenser-side surface temperature: (1) increasing the thermal conduction resistance in the central region of the condenser-side wall and wick, and (2) reducing the vapor core thermal resistance. One way to achieve both effects is to eliminate parts of the wick layer in the central condenser region. This would locally reduce the effective thermal conductivity of the wick in this region by replacing the porous sintered copper with a layer of lower-conductivity liquid (*viz.*, water). In addition, the effective permeability (of the sintered copper wick and the grooves) would increase, which would allow for a thinner wick over the entire condenser side inner wall while maintaining the same pressure drop, and hence reduce the vapor-core thermal resistance. This section explores the potential improvement in temperature uniformity that may be achieved with such a design modification, and the relative benefits of the two mechanisms.

A wick design is evaluated that excises part of the wick material on the condenser side in the region $r < 10$ mm. This region is targeted because of the comparatively high heat flux it experiences before a steep drop-off outside this zone, as shown in Figure 7c. The design consists of radial patterned grooves in the condenser-side wick, as represented in Figure 5d. For this hypothetical case, the pattern has 36 periodic units (of 10 deg each) in the azimuthal direction; in each unit, 90% of the wick area is removed. The resulting pattern looks like a spoked wheel. The grooved condenser wick design otherwise has the same materials and geometry as the baseline design, and the behavior was simulated using the same boundary conditions.

The simulated results are compared in Figure 8 to the baseline (uniform-wick) design. Figure 8c shows that the amount of condensation heat flux at the condenser-side wick-vapor interface in the central region (r < 10 mm) has reduced by a small fraction, which is reflected in the condenser-surface temperature profile (shown in Figure 8a). While the heat flux has a small sharp peak at r = 0, this is smeared due to conduction in the condenser-side wall, and thus it does not have an adverse effect on the condenser-surface temperature profile. This indicates that the thermal resistance of the wick in the central region is increased, and the peak-to-mean temperature difference at the condenser surface has marginally reduced from 6.33 K for the baseline case to 5.96 K for the current design. Figure 8b shows the pressure distribution in the wick. It can be seen that the pressure gradient in the central region of the condenser wick has drastically reduced compared to the baseline case as a result of the increased effectively permeability to liquid flow.

The significant effect caused by a change in the effective wick permeability indicates that (1) it may be possible to achieve a significant reduction in the effective vapor core thermal resistance. In contrast, (2) a relatively small performance improvement is obtainable by increasing the condenser-side conduction resistance in the central region. Thus, a condenser-side wick design is explored in the next section that aims to maximize the benefit of increasing the condenser-side wick effective permeability.

4.3. Biporous condenser-side wick domain design with radially discretized grooves

As demonstrated in section 4.2, the major advantage of a grooved condenser-side wick design lies in the reduced wick pressure drop rather than the increased thermal resistance in the central region. Thus, this design approach need not be restricted to the central region (r < 10

mm), but instead can be extended to the full radius of the condenser-side wick. This extension would further reduce the wick pressure drop, allowing for an even thinner wick layer and lower vapor-core thermal resistance. However, the radial grooves cannot simply be extended from the center to the circumference of the condenser-side wick due to restrictions on the width of the grooves. In the grooves, vapor condenses onto the vapor chamber wall and forms a liquid pool with a meniscus connecting the neighboring strips of sintered copper, as illustrated in Figure 9. If a groove is too wide, the meniscus shape is stretched so that the liquid bridge between adjacent sintered copper strips is broken; condensing liquid may accumulate under these conditions and block the vapor flow. Thus, the width of the groove is limited to a maximum value.

Assuming a circular meniscus with a constant contact angle, we obtain a relation for the maximum groove width for a given wick thickness.

$$W_{\text{limit}} = \frac{2t_{wick}\cos(\theta)}{(1-\sin(\theta))} \tag{9}$$

For a copper-water system with a contact angle of ~40 deg, this minimum width is of the order of 100 μm. If a single groove were to extend from the center of the condenser-side wick to the circumference, where the maximum groove width is restricted to 100 μm, this groove would need an impossibly small angle at the center. The strips of sintered copper wick between grooves must also adhere to a minimum width limit in order to accommodate 3 particle diameters.

These groove width limits are considered in the design of a biporous condenser-side wick with radially discretized grooves, as illustrated in Figure 10. The design has multiple sections, each having equal-length grooves in the radial direction. The number of grooves (and strips of sintered copper between the grooves) contained in each section can then increase for sections further away from the center. This strategy avoids nonviable groove angles at the center, while maintaining the width limits. The angle of the groove within each section is designed such that

the groove reaches the width limit at the maximum radial location in that section. The angle of the sintered copper strips is determined such that their width is at the minimum limit at the minimum radial location in each section. This approach aims to minimize the wick pressure drop. It should be noted that the design does not attempt to increase the thermal resistance of the condenser-side wick in the central region, since the ancillary benefits of doing so are negligible. A small circular section in the center has no grooves based on the minimum possible sintered copper strip thickness.

The vapor chamber behavior was simulated with this biporous condenser-side wick design. To capture the complex geometry of the condenser-side wick domain, an effective permeability formulation was implemented (Appendix A). Using this formulation, the biporous wick design could be simulated as an axisymmetric geometry. A minimum wick thickness is required to minimize the lateral temperature difference in the vapor-core, while satisfying the capillary pressure constraint defined in section 4.1. Hence, the wick thickness was reduced from 30 μm in the baseline case to 21 μm for the biporous wick design. For a design with nine discrete radial sections of 5 mm-long grooves (except for the innermost section, which has 2.5 mm-long grooves), the approach described above resulted in a condenser-side wick with 240, 480, 786, 1080, 1372, 1662, 1951, 2240, and 2529 grooves in each of the radial sections; the central region without grooves has a radius of 2.5 mm. Other than the reduced wick thickness and biporous condenser-side wick design, the rest of the geometry and boundary conditions were the same as the baseline case.

The simulation results comparing the biporous and baseline wick designs are shown in Figure 11. Figure 11b shows the pressure in the wick; the pressure gradient in the condenser-side wick is much lower for the biporous wick design. The thinner biporous wick results in lowered

vapor core thermal resistance, leading to a more uniform temperature profile on the condenser surface. This is reflected in the redistribution of heat flux due to condensation at the wick-vapor interface (Figure 11c). The condenser-surface temperature profile shows a reduction in the peak temperature when compared to the baseline case of 2.33 K (Figure 11a). The peak-to-mean temperature was reduced from 6.33 K to 4 K due with the biporous wick design, a 37% improvement.

5. Conclusions

The performance-enhancement strategies developed in this work provide a pathway for effectively introducing vapor chambers into mobile devices for thermal management. In mobile cooling applications, the ultra-thin form factor, low heat input power, and heat rejection to the ambient by natural convection -- which define the performance-governing transport mechanisms -- have limited the viability of vapor chambers designed using conventional performance metrics. The design approach under such conditions must shift focus away from the traditional objective of reducing the chip/evaporator temperature and instead target improved condenser-surface temperature uniformity, where the effectiveness of the heat spreader directly affects user comfort in mobile platforms.

The design process used a three-dimensional numerical vapor chamber transport model to evaluate various geometries at a high fidelity. The computational cost issues associated with using this numerical model at ultra-thin form factor geometries were identified, and a cost-reducing steady-state-seeking solution algorithm was developed and implemented. This algorithm allowed for an order-of-magnitude reduction in the computational cost.

It was concluded that condenser-surface temperature uniformity is governed by the layout of the condenser-side wick; uniformity can be improved by (1) increasing thermal resistance across the condenser-side wick in the heat input region, and (2) increasing condenser-side wick permeability in order to reduce its thickness, and thereby increase the vapor-core thickness for lowered lateral thermal resistance. A hypothetical design implementing these two strategies was simulated and revealed that the second strategy can yield significant improvement in the condenser-surface temperature uniformity. A biporous condenser-side wick design was developed on this principle; numerical simulations comparing the baseline and biporous consider-side wick designs showed that the peak-to-mean condenser surface temperature difference of the vapor chamber could be reduced by up to 37%. The approach developed in this work can be adopted to produce vapor chamber wick designs in coordination with practical fabrication constraints.

Acknowledgement

The authors thank Intel Corporation, specifically Program Director Mondira Pant (Intel Labs, University Collaborative Research) and Project Mentor Mark MacDonald, for their support of this work as part of the Intel Strategic Research Alliance (ISRA) on platform thermal cooling solutions.

References

[1] J. A. Weibel and S. V. Garimella, Recent advances in vapor chamber transport characterization for high-heat-flux applications, Advances in Heat Transfer, vol. 45, pp. 209–301, 2013.

[2] Q. Cai and Y.-C. Chen, Investigations of biporous wick structure dryout, Journal of Heat Transfer, vol. 134, no. 2, 021503, 2011.

[3] J. A. Weibel and S. V. Garimella, Visualization of vapor formation regimes during capillary-fed boiling in sintered-powder heat pipe wicks, International Journal of Heat and Mass Transfer, vol. 55, no. 13–14, pp. 3498–3510, 2012.

[4] T. Semenic and I. Catton, Experimental study of biporous wicks for high heat flux applications, International Journal of Heat and Mass Transfer, vol. 52, no. 21–22, pp. 5113–5121, 2009.

[5] R. Ranjan, S. V. Garimella, J. Y. Murthy, and K. Yazawa, Assessment of nanostructured capillary wicks for passive two-phase heat transport, Nanoscale and Microscale Thermophysical Engineering, vol. 15, no. 3, pp. 179–194, 2011.

[6] J. A. Weibel, S. V. Garimella, J. Y. Murthy, and D. H. Altman, Design of integrated nanostructured wicks for high-performance vapor chambers, IEEE Transactions on Components, Packaging and Manufacturing Technology, vol. 1, no. 6, pp. 859–867, 2011.

[7] Y. S. Ju, M. Kaviany, Y. Nam, S. Sharratt, G. S. Hwang, I. Catton, E. Fleming, and P. Dussinger, Planar vapor chamber with hybrid evaporator wicks for the thermal management of high-heat-flux and high-power optoelectronic devices, International Journal of Heat and Mass Transfer, vol. 60, pp. 163–169, 2013.

[8] G. S. Hwang, Y. Nam, E. Fleming, P. Dussinger, Y. S. Ju, and M. Kaviany, Multi-artery heat pipe spreader: experiment, International Journal of Heat and Mass Transfer, vol. 53, no. 13–14, pp. 2662–2669, 2010.

[9] Y. Yadavalli, J. A. Weibel, and S. V. Garimella, Performance-governing transport mechanisms for heat pipes at ultrathin form factors, IEEE Transactions on Components, Packaging and Manufacturing Technology, vol. 5, no. 11, pp. 1618–1627, 2015.

[10] H. Aoki, N. Shioya, M. Ikeda, and Y. Kimura, "Development of ultra thin plate-type heat pipe with less than 1 mm thickness," in 26th Annual IEEE Semiconductor Thermal Measurement and Management Symposium (SEMI-THERM), Santa Clara, CA, 2010, pp. 217–222,.

[11] C. Ding, G. Soni, P. Bozorgi, B. D. Piorek, C. D. Meinhart, and N. C. MacDonald, A flat heat pipe architecture based on nanostructured titania, Journal of Microelectromechanical Systems, vol. 19, no. 4, pp. 878–884, 2010.

[12] C. Oshman, B. Shi, C. Li, R. Yang, Y. C. Lee, G. P. Peterson, and V. M. Bright, The development of polymer-based flat heat pipes, Journal of Microelectromechanical Systems, vol. 20, no. 2, pp. 410–417, 2011.

[13] R. Lewis, S. Xu, L. Liew, C. Coolidge, R. Yang, and Y. Lee, Thin flexible thermal ground planes: fabrication and scaling characterization, Journal of Microelectromechanical Systems, vol. 24, no. 6, pp. 2040–2048, 2015.

[14] G. Wagner and W. Maltz, Thermal management challenges in the passive cooling of handheld devices, in 19th International Workshop on Thermal Investigations of ICs and Systems (THERMINIC), Berlin, Germany, 2013, pp. 344–347.

[15] U. Vadakkan, S. V. Garimella, and J. Y. Murthy, Transport in flat heat pipes at high heat fluxes from multiple discrete sources, Journal of Heat Transfer, vol. 126, no. 3, pp. 347–354, 2004.

[16] R. Ranjan, J. Y. Murthy, S. V. Garimella, D. H. Altman, and M. T. North, "Modeling and Design Optimization of Ultra-Thin Vapor Chambers for High Heat Flux Applications," IEEE Transactions on Components, Packaging and Manufacturing Technology, Vol 2(9), pp. 1465-1479, 2012.

[17] R. W. Schrage, A theoretical study of interphase mass transfer, Columbia University Press, New York, 1953.

[18] R. Marek and J. Straub, Analysis of the evaporation coefficient and the condensation coefficient of water, International Journal of Heat and Mass Transfer, vol. 44, no. 1, pp. 39–53, 2001.

[19] Fluent, ANSYS FLUENT 14.0 User's Guide, ANSYS Fluent, Canonsburg, PA, 2011.

[20] R. Ranjan, J. Y. Murthy, S. V. Garimella, and U. Vadakkan, A numerical model for transport in flat heat pipes considering wick microstructure effects, International Journal of Heat and Mass Transfer, vol. 54, no. 1–3, pp. 153–168, 2010.

[21] G. Patankar, S. Mancin, J. A. Weibel, S. V. Garimella, and M. A. MacDonald, A method for thermal performance characterization of ultra-thin vapor chambers cooled by natural convection, Journal of Electronic Packaging, vol. 138, no. 1, pp 010903, 2016.

[22] A. Faghri, Heat pipe science and technology, Washington DC: Taylor & Francis, 1995.

Appendix*:* Effective permeability formulation

In the condenser-side wick, liquid flows radially outward. The biporous wick design has alternating grooves and sintered copper strips in the azimuthal direction. Liquid flows in parallel through these regions. The governing momentum equations for fluid flow though porous media are shown in equations (2-4). The last two terms on the right hand side represent additional viscous and inertial pressure drop due to the porous medium. The liquid velocities are sufficient low in the current study such that the inertial pressure drop is negligible and the additional viscous pressure drop is given by

$$\frac{dP}{dx} = \frac{\mu}{K_1} u_1 = \frac{\mu}{K_2} u_2 \qquad (10)$$

where 1 and 2 refer to the permeability of sintered copper powder strips and rectangular grooves, respectively. The permeabilities are computed using empirical correlations found in Ref. [22]. An effective liquid velocity can be defined as follows.

$$u_1 A_1 + u_2 A_2 = u_{eff}\left(A_1 + A_2\right) \tag{11}$$

Combining equations (10) and (11) yields the following relation,

$$\frac{dP}{dx} = \frac{\mu}{K_1 A_1 + K_2 A_2} u_{eff}\left(A_1 + A_2\right) = \frac{\mu}{K_{eff}} u_{eff}$$
$$K_{eff} = \frac{K_1 A_1 + K_2 A_2}{A_1 + A_2} \tag{12}$$

which defines the effective permeability of the wick as the area-weighted average of the individual permeabilities. Note that the areas are normal to the radially outward flow direction. The validity of this effective permeability formulation was confirmed by simulating (FLUENT [19]) flow through a representative periodic unit cell geometry containing one sintered powder strip and one adjacent groove, with a pressure drop imposed across the radial ends of the geometry. An effective permeability was computed based on the pressure drop, total flow rate, and viscosity of the fluid. This computed permeability was compared to the area-weighted average of the individual permeabilities (Equation (12)). The error in the area-averaged effective permeability was less than 5%.

List of Figures

Figure 4. Schematic representation of vapor chamber condenser-surface temperature profile (inset shows the boundary conditions). Performance improvement is measured as a reduction of the peak-to-mean surface temperature.

Figure 5. (a) Geometry and boundary conditions for the baseline design of the vapor chamber and (b) an axisymmetric section showing internal layout of the wick and vapor domains. Magnified details of the wick and vapor layout for (c) baseline case and (d) grooved condenser wick domain design.

Figure 6. Results for the baseline, uniformly distributed wick case: contours of (a) temperature (dimensions in the plot are scaled by 20× along the thickness), (b) velocity magnitude in the wick, (c) pressure in the wick, (d) velocity in the vapor core, (e) pressure in the vapor core (parts (b) through (e) are scaled by 90× along the thickness relative to the radius).

Figure 7. Results for the baseline, uniformly distributed wick case: plots of the radial distribution of (a) temperature and heat flux on the outer condenser-side surface, (b) pressure in the wick, and (c) heat flux due to condensation at the condenser-side wick-vapor interface.

Figure 8. Results for the case with the grooved condenser-side wick domain design: plots of the radial distribution of (a) temperature and heat flux on the outer condenser-side surface, (b) pressure in the wick, and (c) heat flux due to condensation at the condenser-side wick-vapor interface.

Figure 9. Illustration of the groove width restriction

Figure 10. Illustration of the biporous condenser-side wick domain design with radially discrete grooves. The illustration is shown for a wick with three radial sections; the geometry details are not shown to scale.

Figure 11. Results for the case with the biporous condenser-side wick domain design: plots of the radial distribution of (a) temperature and heat flux on the outer condenser-side surface, (b) pressure in the wick, and (c) heat flux due to condensation at the condenser-side wick-vapor interface.

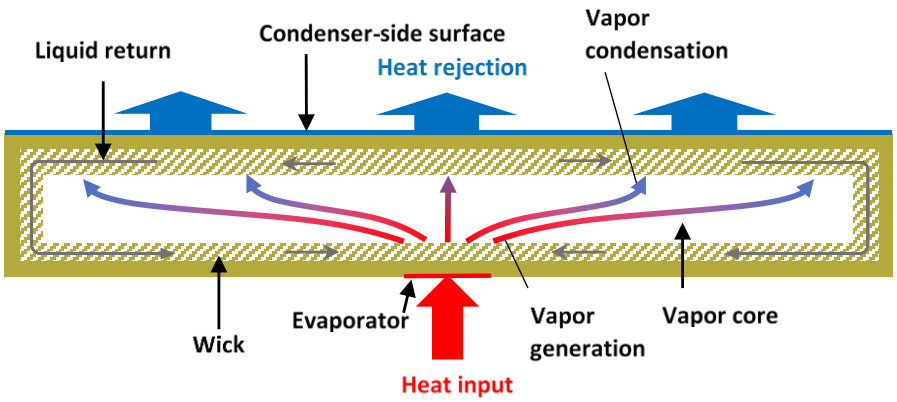

Figure 1. Schematic diagram of vapor chamber operation.

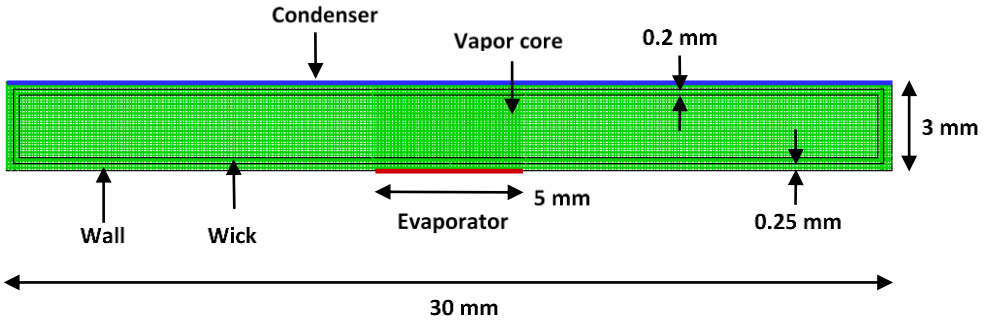

Figure 2. 2D vapor chamber geometry and mesh details for example case used to verify the behavior and effectiveness of the steady-state-seeking solution algorithm.

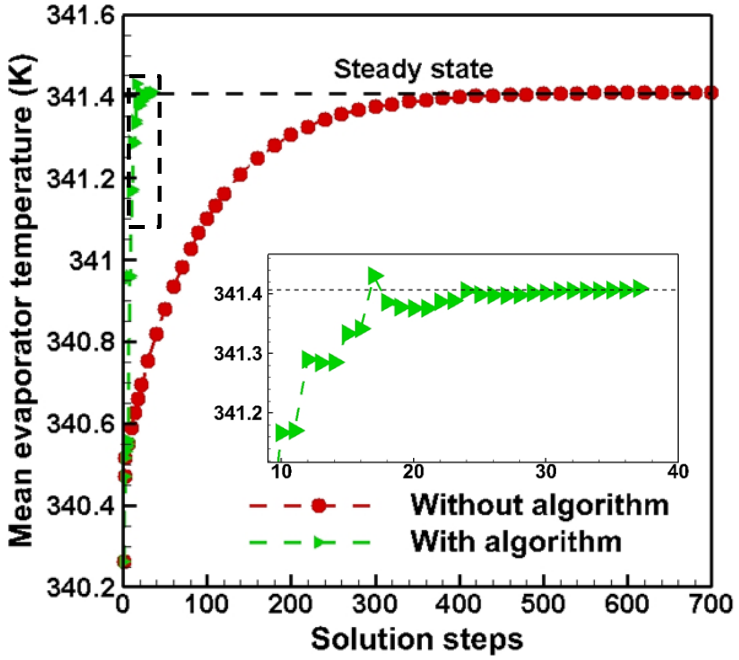

(a)

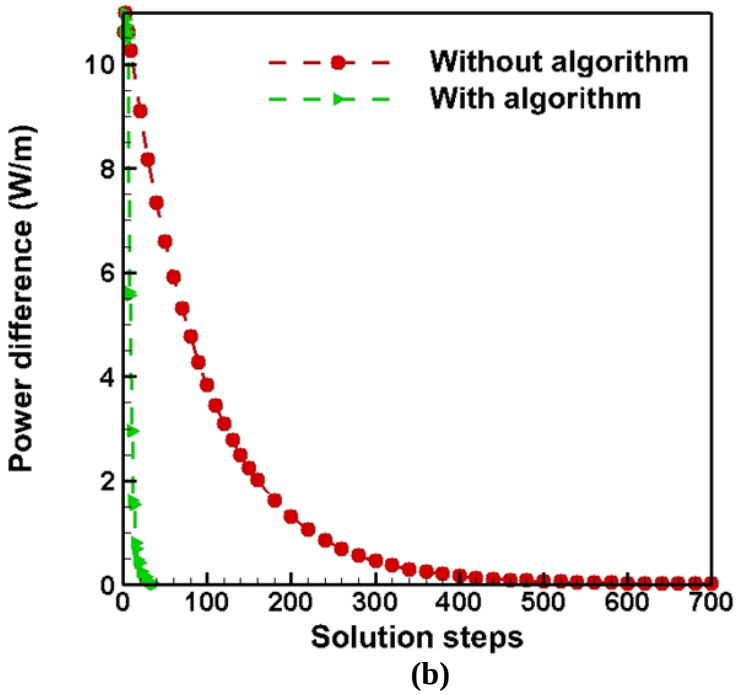

(b)

Figure 3. Progression of the (a) mean evaporator temperature (inset shows dashed region at the top left) and (b) evaporator-to-condenser power difference with solution steps for the full transient simulation and with the steady-state-seeking solution algorithm implemented.

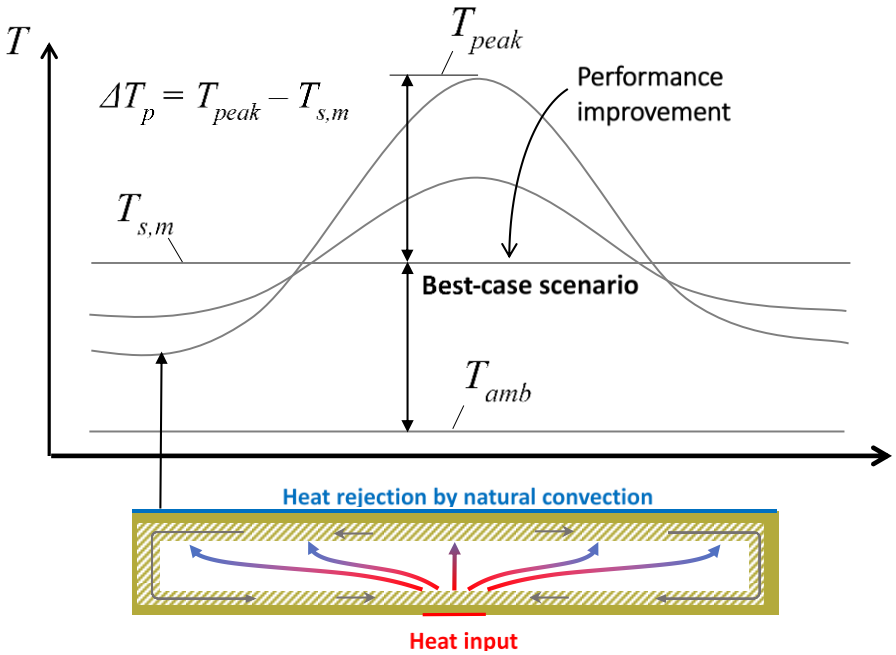

Figure 4. Schematic representation of vapor chamber condenser-surface temperature profile (inset shows the boundary conditions). Performance improvement is measured as a reduction of the peak-to-mean surface temperature.

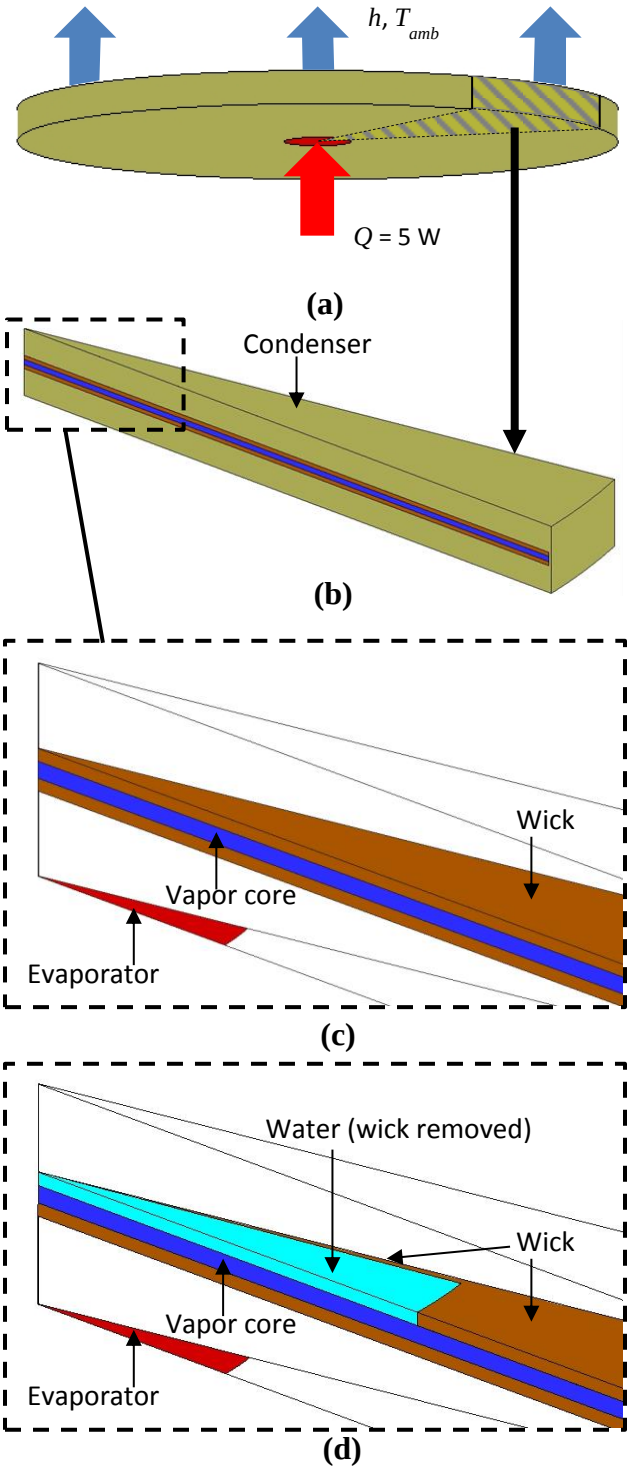

Figure 5. (a) Geometry and boundary conditions for the baseline design of the vapor chamber and (b) an axisymmetric section showing internal layout of the wick and vapor domains. Magnified details of the wick and vapor layout for (c) baseline case and (d) grooved condenser wick domain design.

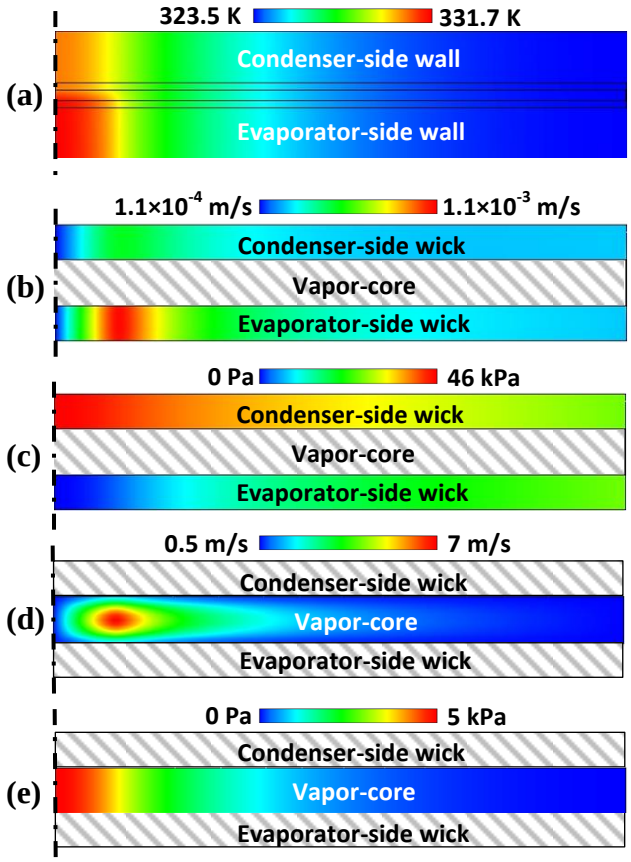

Figure 6. Results for the baseline, uniformly distributed wick case: contours of (a) temperature (dimensions in the plot are scaled by 20× along the thickness), (b) velocity magnitude in the wick, (c) pressure in the wick, (d) velocity in the vapor core, (e) pressure in the vapor core (parts (b) through (e) are scaled by 90× along the thickness relative to the radius).

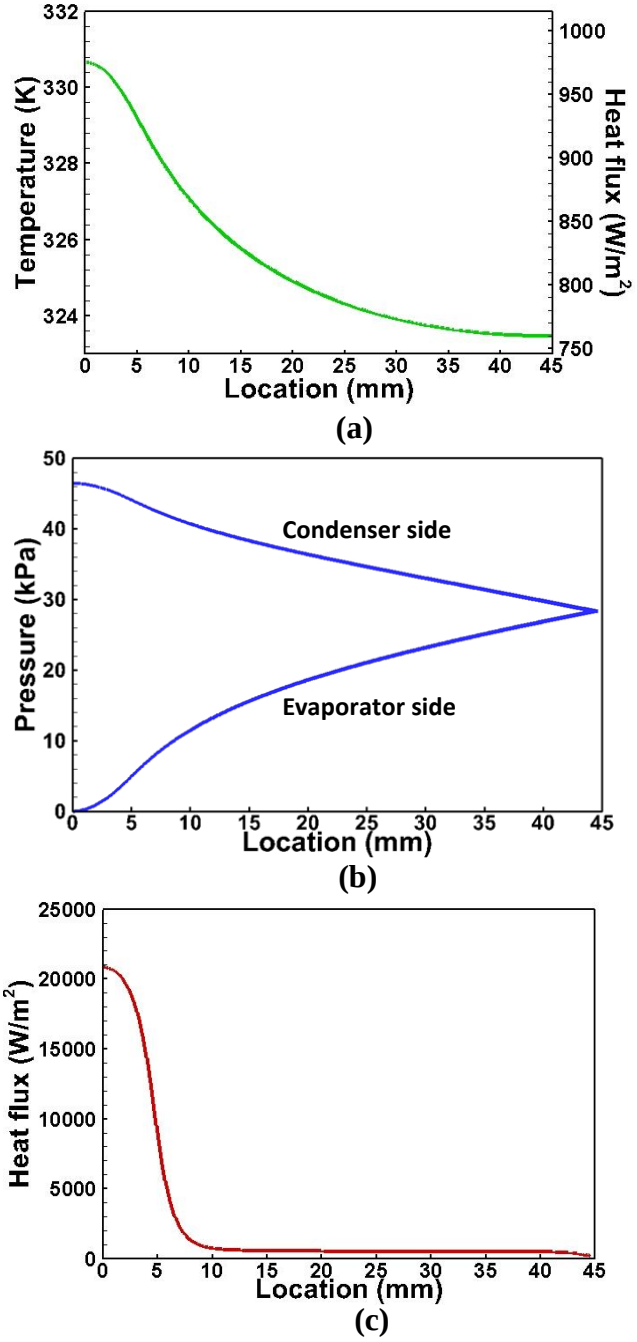

Figure 7. Results for the baseline, uniformly distributed wick case: plots of the radial distribution of (a) temperature and heat flux on the outer condenser-side surface, (b) pressure in the wick, and (c) heat flux due to condensation at the condenser-side wick-vapor interface.

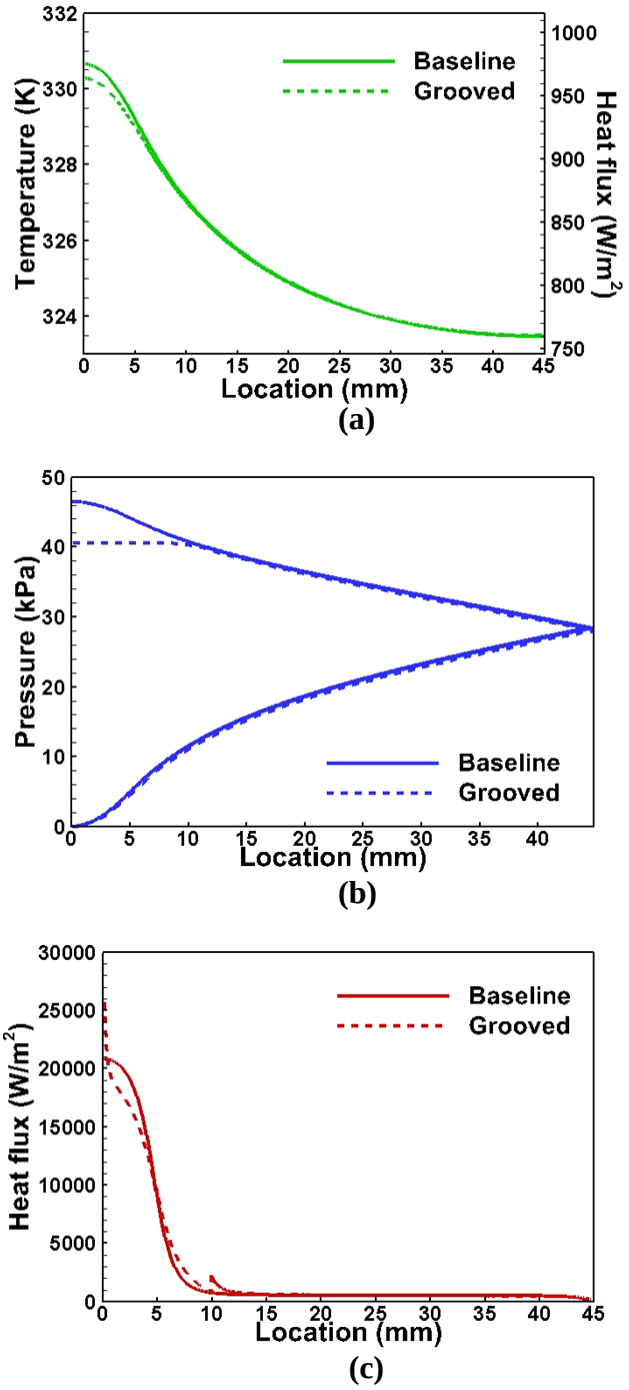

Figure 8. Results for the case with the grooved condenser-side wick domain design: plots of the radial distribution of (a) temperature and heat flux on the outer condenser-side surface, (b) pressure in the wick, and (c) heat flux due to condensation at the condenser-side wick-vapor interface.

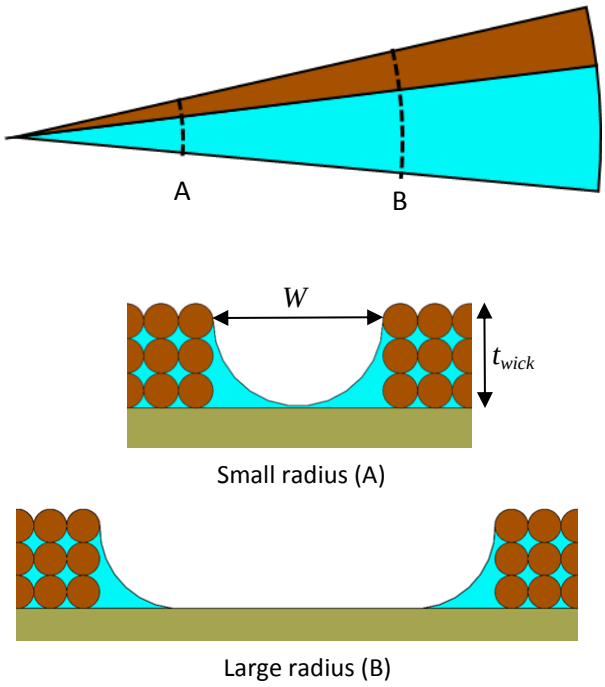

Figure 9. Illustration of the groove width restriction.

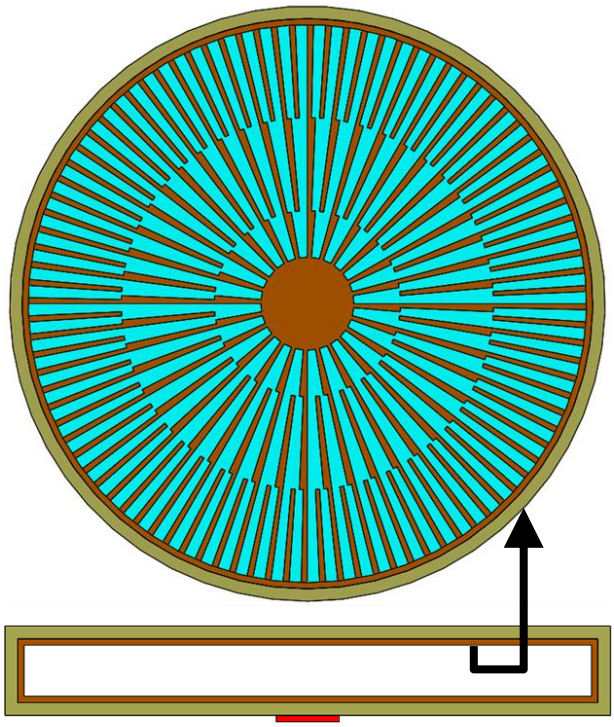

Figure 10. Illustration of the biporous condenser-side wick domain design with radially discrete grooves. The illustration is shown for a wick with three radial sections; the geometry details are not shown to scale.

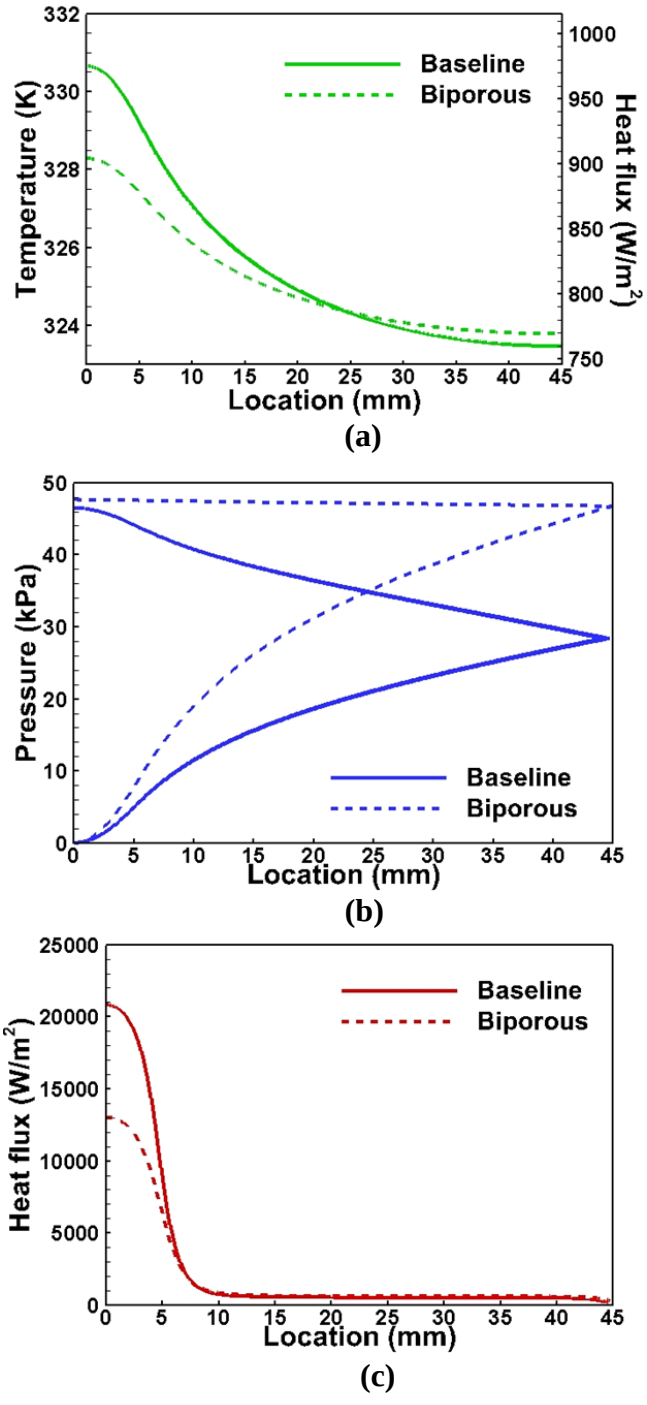

Figure 11. Results for the case with the biporous condenser-side wick domain design: plots of the radial distribution of (a) temperature and heat flux on the outer condenser-side surface, (b) pressure in the wick, and (c) heat flux due to condensation at the condenser-side wick-vapor interface.